

Microstructure and Electrochemical Properties of Refractory Nanocrystalline Tantalum-based Alloys

J. Jakubowicz^{1,}, G. Adamek¹, M. Sopata¹, J.K. Koper¹, T. Kachlicki¹, M. Jarzebski³*

¹ Poznan University of Technology, Institute of Materials Science and Engineering, Jana Pawla II, 24, 61-138 Poznan, Poland

² Life Sciences University, Department of Physics, Wojska Polskiego 38/42, 60-637 Poznan, Poland

*E-mail: jaroslaw.jakubowicz@put.poznan.pl

Received: 3 October 2017 / *Accepted:* 26 November 2017 / *Published:* 28 December 2017

The nanocrystalline refractory tantalum alloys were made using mechanical alloying. The tantalum alloys were modified by niobium, molybdenum and tungsten in the concentration of 5, 10, 20 and 40 wt.%. The nanocrystalline powders were consolidated (hot-pressed) using the pulse plasma sintering mode. The hot pressing at the temperature of 1300°C results in an increase of the grain size, in comparison to mechanically alloyed powders. However, the lowest grain size (significantly below 100 nm) was achieved for Ta-W alloys (approximately 40-60nm). The grain size was confirmed by XRD, TEM and AFM. The most uniform microstructure is also exhibited by the Ta-W alloys. The corrosion resistance was measured using the potentiodynamic mode in a chloride solution. The nanocrystalline Ta-Mo and Ta-W alloys achieved the same level of corrosion resistance as microcrystalline pure tantalum and 3 orders of magnitude better than pure nanocrystalline tantalum. Among all the prepared nanocrystalline tantalum alloys, the most promising properties exhibit those having 10% of the tungsten addition.

Keywords: Tantalum nanocrystalline alloys; refractory metals; mechanical alloying; pulse plasma sintering; corrosion resistance

1. INTRODUCTION

Tantalum is a refractory element of high melting point and toughness. It belongs to a group of materials of many possible applications, from temperature resistant to biomedical ones [1-3]. The material is very resistant to corrosive agents as well high temperature and radiation [4, 5]. The limits for its application are related mainly to its high cost and difficult processing. The material is promising

for future applications conditional upon its technological progress. Tantalum constitutes a base for its refractory alloys and composites [6-8]. It can also be used for coating other materials [9]. Tantalum is a ductile bcc metal of high melting point that can be strengthened through grain size reduction and alloying without brittle fracture. The alloying elements, which can modify the properties of tantalum, can be derived into interstitial or substitutional elements, such as C, N or W, Mo, Nb and Ti, respectively. Tungsten, for example, has a high melting point, strength and corrosion resistance, yet brittle material. Combination of different elements with tantalum results in solid solution and/or precipitation strengthening [6]. A solute-solution softening is possible resulting in a decreased yield stress [10]. Tantalum exhibits significant strain hardening, which is a function of the strain rate and pre-straining. In the form of nanostructure, tantalum tends to get softer at high strain rates [11]. Ductility and flow stress increase when the grain size is lower than 100 nm.

Beside solid solutions, intermetallic phases lead to the strengthening of the microstructure. It is very difficult to prepare uniform alloys using conventional melting processes (for example, vacuum arc melting or electron beam melting) and casting, especially if the melted components have significantly different melting temperatures (high melting temperature of 3017°C for Ta) and densities (high density of 16.4 g/cm³ for Ta).

In conventionally cast tantalum, the microstructure contains large columnar and highly textured grains [12, 13]. Subsequent plastic deformation of the textured microstructure is often hampered by a non-uniform flow [14, 15]. The texture requires many processing routes to its elimination and uniformization [12-15]. The conventional melting processes of refractory alloys require equipment capable of maintaining a very high temperature. To overcome these problems, the refractory compounds can be made using unconventional processes, leading to the formation of powders, bulks or coatings often in the form of nanomaterials [16, 17].

The formation of tantalum alloys in the form of nanopowders can be done through intensive milling of the elemental powder mixture in the process of mechanical alloying (MA). The problem related to nanocrystalline powders is their transformation into bulk consolidated material as well as the oxidation process. The high consolidation temperature leads to grain growth, which is why conventional powder metallurgy including conventional high-temperature and long-time sintering has limited applications. Several processes useful for nanomaterials consolidation have been developed, in which the consolidation temperature and time are limited [18-23]. The nanocrystalline powders have better sinterability and require lower consolidation temperature in comparison to the microcrystalline ones [11, 24]. The lowest useful consolidation temperature is limited by excess high porosity and low mechanical strength of the final product, whereas the highest consolidation temperature is limited by the excess grain growth. The large surface area of the nanoparticles improves the densification process. Unfortunately, the large and highly reactive surface area of the active metals exposed to oxygen (even residual oxygen at vacuum or inert atmosphere) leads to fast oxidation and reduction of mechanical properties [25].

Due to lack of information regarding nanostructural tantalum alloys, this work shows the results of the formation and properties of nanocrystalline Ta-based alloys modified by refractory Nb, Mo and W elements. The alloys were produced in a mechanical alloying process and the consolidation

was performed by the Pulse Plasma Sintering (PPS) process. The structural and electrochemical properties of the alloys were described.

2. MATERIAL AND METHODS

In this work, nanocrystalline Ta-Nb, Ta-Mo and Ta-W alloys, containing 5, 10, 20 and 40 wt.% of Nb, Mo and W were synthesized, marked as Ta-xNb, Ta-xMo and Ta-xW, where x is 5, 10, 20 or 40 wt.%, respectively. The nanocrystalline tantalum alloy powders were produced by mechanical alloying (MA). The tantalum powder of the 325 mesh size ($<44\ \mu\text{m}$) and the purity $>99.97\%$ was provided by Alfa Aesar (Germany). The niobium powder $<45\ \mu\text{m}$ size and purity $>99.8\%$ as well as tungsten powder of the size range $0.1\text{-}1\ \mu\text{m}$ and purity $>99.9\%$ were provided by Sigma-Aldrich (Germany). The molybdenum powder of the size $<5\ \mu\text{m}$ and purity $>99.8\%$ was provided by Goodfellow (England). The mixture of a total of 5.5g of the powders was loaded and reloaded into the milling vial in the Labmaster and Unilab glove boxes (MBraun, Germany) providing high purity inert atmosphere (argon) of controlled oxygen and moisture content ($<2\ \text{ppm}$). For each alloy several syntheses were performed to provide material for 5 consolidated samples of each designed composition. The MA process was performed in a proprietary hardened steel vial ($>62\ \text{HRC}$) mounted in the SPEX 8000M Mixer/Mill (Spex SamplePrep, USA). The milling time was set experimentally at 48h and the mill ran with the frequency of 875 cycles/minute. A room temperature was a standard condition of the MA process. The steel hardened ball bearings ($>62\ \text{HRC}$) to powder weight ratio was 3. The atmosphere in the vial was inert, of the same purity as in the glove box.

The as-milled powders were then axially hot-pressed at vacuum (about 4 Pa) using graphite die and graphite movable punches. The pressure of the punches directed at the powder was 50 MPa. The boron-nitride spray (HeBoCoat, Germany) was applied to prevent the powder material from sticking to the die and to ensure easier motion of the punches. In the consolidation process, Pulse Plasma Sintering mode (PPS) was applied for heating with pulses of high electric current going through the die and the powder. The hot-pressed equipment including PPS module has been made by Elbit (Elbit, Koszyce Wielkie, Poland). The current pulses in the module were generated by discharging of a 250 μF capacitor, charged to 8 kV maximum voltage. The pulse duration in the sintering process was automatically controlled following a temperature measurement by a pyrometer aiming at the upper punch. Voltage, pulse frequency, force, temperature, and real-time vacuum were automatically controlled during the PPS procedure. The pressing temperature was set experimentally and the process was performed at 1300°C . The time of sintering at a constant temperature was 5 s. The hot-pressed bulk samples were 8 mm in diameter and 4 mm in height.

The structure analysis was performed on each step of the experiments using Empyrean XRD (Panalytical, The Netherlands) equipped with a crystallographic ICDD-JCPDS database. The investigations were carried out using $\text{CuK}\alpha$ radiation at the voltage of 45 mV and the anode current of 40 mA. The structure was investigated in 2θ range $30\text{-}120\ \text{deg.}$, the step size was $0.0167\ \text{deg.}$ and the time per step was 12.54 s/step. The grain size of the alloys was estimated by the Scherrer equation. For the XRD analysis, Panalytical HighScore software was used.

The microstructure and morphology of the powders and alloys was analyzed using Vega 5135 SEM (Tescan, Czech Republic), operating at 20 kV in the mode of secondary electrons. The SEM operates together with PGT Prism 200 Avalon EDS (Princeton Gamma-Tech, USA). The microstructure and grain size analysis was also performed using Q-Scope 250 AFM (Quesant, USA). The AFM worked in the tapping mode using a NanoandMore premounted SSS-NCLR Nanosensors probe of the frequency of 145 kHz and the scan speed of 3 lines/s. A total of 1024 scan lines were fixed for image acquisition. For microstructural observations, all the bulk samples after hot pressing were grinded on a sandpaper (up to 1000 grit), polished in a Al₂O₃ suspension and finally etched in a H₂SO₄ + HNO₃ + HF mixture to reveal the grain boundaries (for the corrosion and XRD tests, the samples were not etched).

A CM 20 Super Twin TEM microscope (Philips, The Netherlands) of a 0.24 nm resolution at an acceleration voltage of 200 kV was applied for the powders characterization.

The hydrodynamic diameters of the particles after the MA process were obtained applying the dynamic light scattering technique (DLS) using Zetasizer Nano-ZS (Malvern Instruments Ltd, UK). Typically, a few mg of the prepared powders were suspended in 1mL of deionized water. Before the examinations, the dispersions were treated at the sonic bath for 2h. For the measurements, 100μL of the supernatant from the suspension was taken into 1000μL of water.

The corrosion resistance was measured on hot-pressed samples using a Solartron 1285 Potentiostat (Solartron Analytical, England). The potentiodynamic mode was applied, starting at -0.5V and finishing at 3V against OCP (open-circuit-potential). The scan rate was 0.5 mV/s. The sample was the working electrode, graphite was the counter electrode and Ag/AgCl was the reference electrode in the electrochemical EG&G electrochemical cell (Princeton Applied Research, USA). The corrosion resistance was measured in the Ringer's solution containing the following concentration of ions: 147.2 mmol·l⁻¹ Na⁺, 4.0 mmol·l⁻¹ K⁺, 2.2 mmol·l⁻¹ Ca²⁺, 155.7 mmol·l⁻¹ Cl⁻. The electrolyte was mixed with a magnetic stirrer and purged with nitrogen.

3. RESULTS

In the described work, nanocrystalline tantalum alloys were made utilizing the mechanical alloying (MA) process, followed by hot pressing using the pulse plasma sintering mode (PPS). For clear comparison of the effect of the alloying elements on the alloy properties, the authors made alloys of identical wt.% content of the Nb, Mo and W as the alloying element (i.e. 0, 5, 10, 20 and 40%). These are substitutional elements forming continuous solid solutions in the entire range of compositions and belong to a group of refractory metals. The main contamination of the elemental powders is oxygen (<1200 ppm), niobium (<50 ppm) and iron (<40 ppm). In the MA process, the powder mixture of desired composition was mechanically milled for 48h. The time of milling was set based on our previous research on the milling of pure Ta [26] as well as on the experiments of the current work for alloy formation. During intensive milling of the powders in the steel vial, the iron contamination was introduced into the alloy composition (Fig. 1). Oxygen and carbon in alloys

(introduced from the atmosphere and graphite die, respectively) were detected by EDS (not shown here), but their content cannot be properly determined using this method.

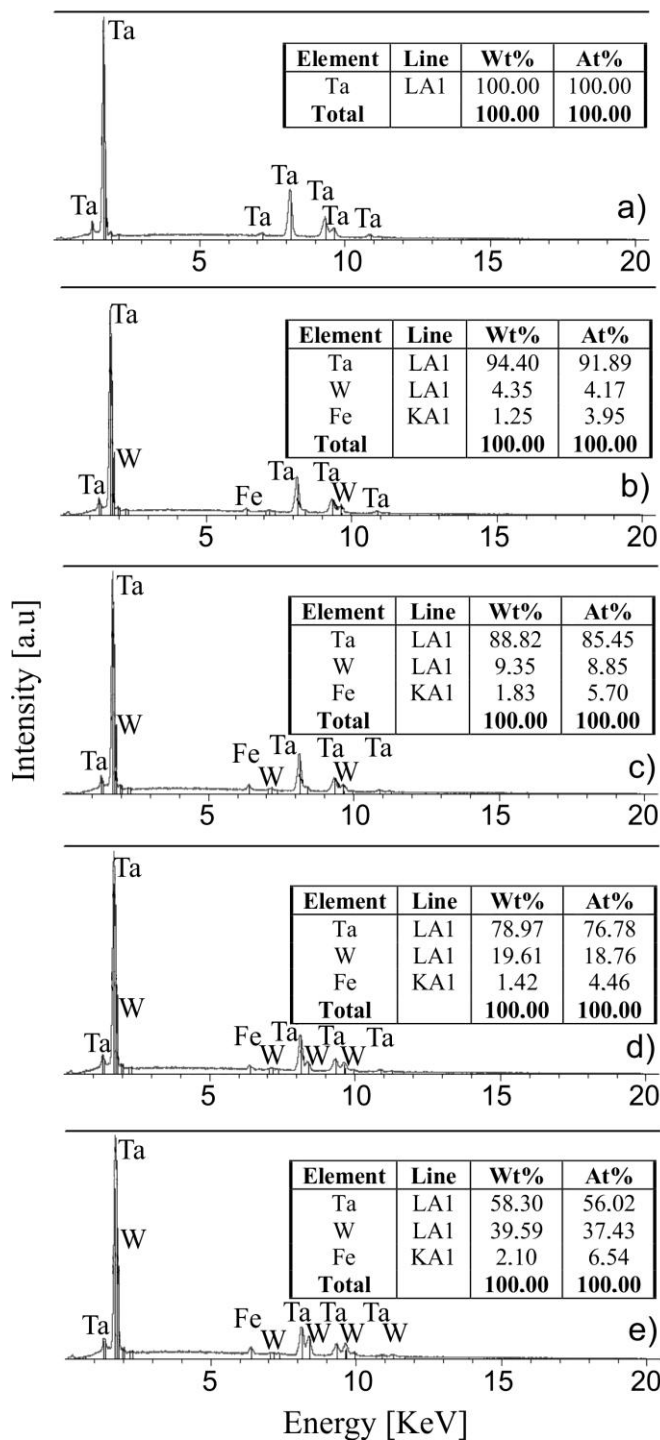


Figure 1. Example EDS analysis of the material after mechanical alloying and hot pressing for the: Ta (a), Ta-5W (b), Ta-10W (c), Ta-20W (d) and Ta-40W (e) designed compositions

In the process, the authors used Ar of 99.999% purity at all experimental stages, thus the oxygen content was limited. In the work [27] the authors used depth profiling AES analysis for chemical analysis of the mechanically alloyed powders. The thickness of the oxide layer reaches 5 nm,

whereas for iron and carbon it is approx. 10 nm, hence the powders in the mechanical alloying process are contaminated only in the surface layer [33]. The final alloy composition after mechanical alloying and hot pressing is slightly different from the design composition, because of the iron impurity (Fig. 1). In all the alloys, the Fe content does not exceed 2.1 wt.%.

Figure 2 shows the XRD spectra for microcrystalline Ta (a), example Ta-40Nb composition after the MA process (b) and examples of Ta-40Nb, Ta-40Mo and Ta-40W alloys of the highest alloying elements content after the MA and PPS processes (c, d, e). For all the investigated alloys the solid solutions are formed. The hot pressing of the mechanically alloyed powders leads to their densification and consolidation. The graphite die can partially react with the powder, forming carbides. The formation of carbides while pressing in the graphite die was also observed in [22]. The hot pressing in all the cases results in narrower and higher intensity XRD peaks, which means that the grain size increases during high temperature consolidation.

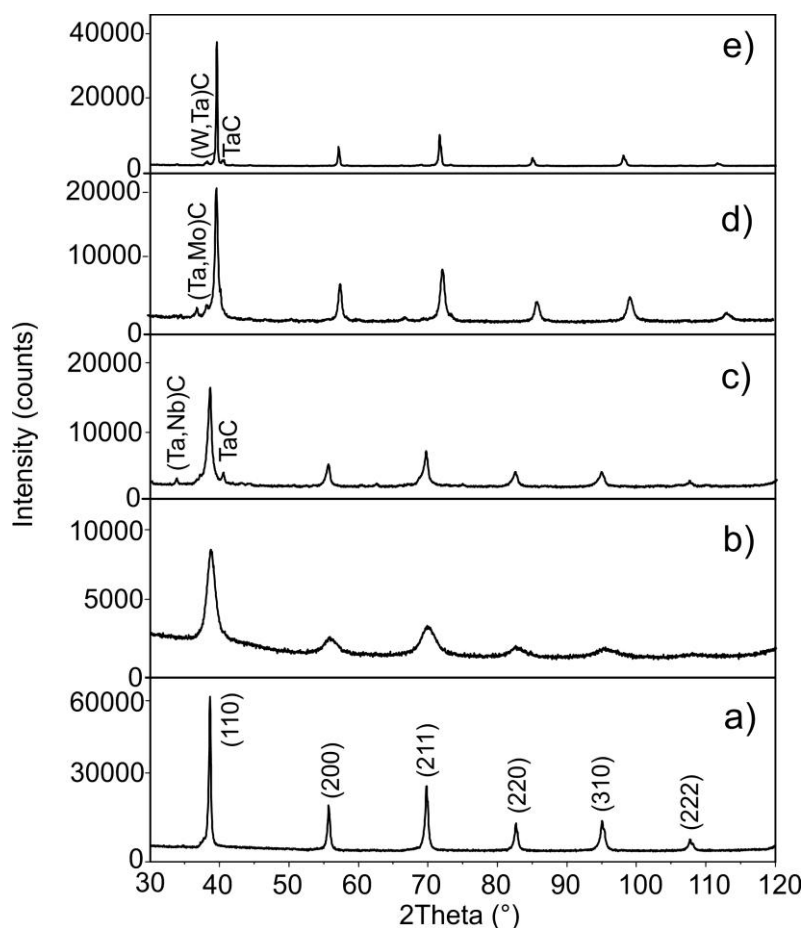


Figure 2. XRD of pure Ta (a), example Ta-40Nb after mechanical alloying (b), and example bulk alloys Ta-40Nb (c), Ta-40Mo (d) and Ta-40W (e) after mechanical alloying and PPS (c-e)

Mechanical alloying leads not only to alloy formation at a room temperature, but also to a significant reduction of the grain size (Figure 3; data obtained based on the XRD spectra using Panalytical HighScore software).

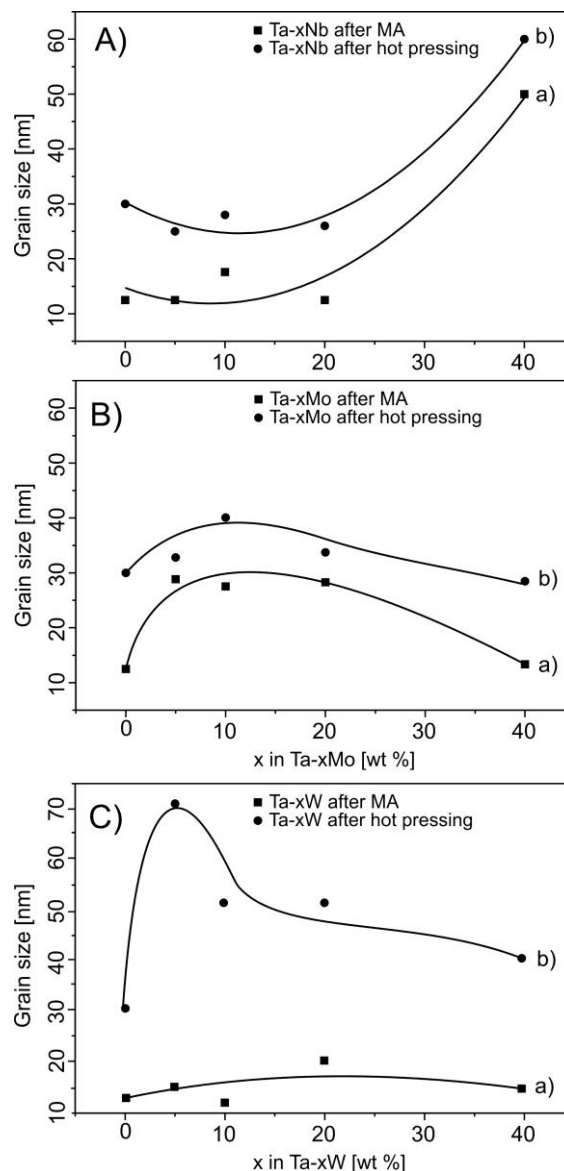


Figure 3. The effect of the Nb (A), Mo (B) and W (C) content on the grain size of the Ta-xNb, Ta-xMo and Ta-xW alloys after mechanical alloying (a) and hot pressing (b)

In all alloys a nanostructure was formed, i.e. there exist grains with the size significantly below 100 nm. In the Ta-Nb system, after the MA process, the grain size increases with the Nb content, and for Ta-40Nb reaches approx. 48 nm, whereas pure Ta after 48h milling has grains of approx. 13 nm (Fig. 3A). Hot pressing, as was shown on the XRD spectra, results in a grain size increase, and for pure nanocrystalline Ta and Ta-40Nb alloys, the values are 30 and 60 nm, respectively (Fig. 3A). For the Ta-Mo alloy system, the increase of the Mo content up to 10% initially leads to an increase in the grain size, whereas at a higher Mo content, the size decreases (Fig. 3B). The hot-pressed Ta-Mo alloys have a lower grain size in comparison to the Ta-Nb alloys (Fig. 3B). After hot pressing, the grain size does not exceed 40 nm. For the Ta-W alloy system, for all investigated tungsten contents, the MA process results in a grain size of the range of 12-20 nm (Fig. 3C). After hot pressing, the grain size

significantly increases for the Ta-5W alloy only and reaches 70 nm. For higher tungsten content, the material has a grain size of approx. 40-50 nm.

The hydrodynamic diameters of the particles (Fig. 4) after mechanical alloying were obtained with dynamic light scattering (DLS). The average values were obtained from 10 measurements and representative particle size distributions. In the mechanical alloying, due to the milling characteristic, mainly the agglomerates are formed composed of smaller grains (see later TEM results in Fig. 5).

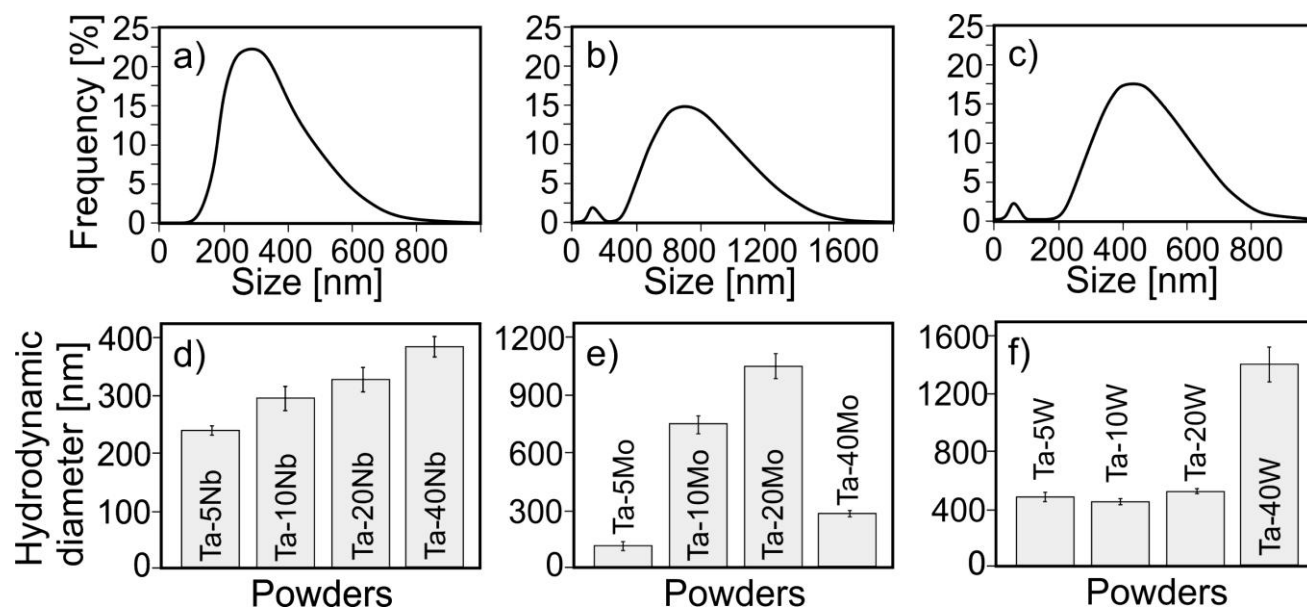


Figure 4. Example DLS particle size distribution of the Ta-10Nb (a), Ta-10Mo (b) and Ta-10W sample (c) and the average hydrodynamic size of particles (agglomerates) of the Ta-Nb (d), Ta-Mo (e) and Ta-W (f) powders

These agglomerates are stable even upon sonication. For pure nanocrystalline Ta, the agglomerate size was 269 nm (not shown in Fig. 4), whereas for the Ta-Nb alloys, the agglomerate size (hydrodynamic equivalent diameter) increased from 236 nm for the Ta-5Nb to 380 nm for the Ta-40Nb powders. Among the Ta-Mo powders, for Ta-5Mo, the agglomerates reached the lowest value of 130 nm, whereas for the Ta-W system, the agglomerates were significantly larger and for 5-20% of tungsten they were kept at the level of approx. 400 nm and significantly increased up to 1414 nm for the 40% W content.

The selected powders of the Ta and Ta-Nb alloys after the MA process were visualized using TEM (Fig. 5). TEM confirmed the nanostructure in the extensively milled materials (grain size <100 nm). TEM showed that the nanocrystalline Ta powder had a grain size of approx. 20 nm, Ta-5Nb, Ta-20Nb and Ta-40Nb had a grain size of 80 nm, 40 nm and 90 nm, respectively. The correlation of the TEM with the XRD results is quite good. The grain size estimated using TEM was slightly higher, but more tangible and reliable in comparison to those obtained using XRD.

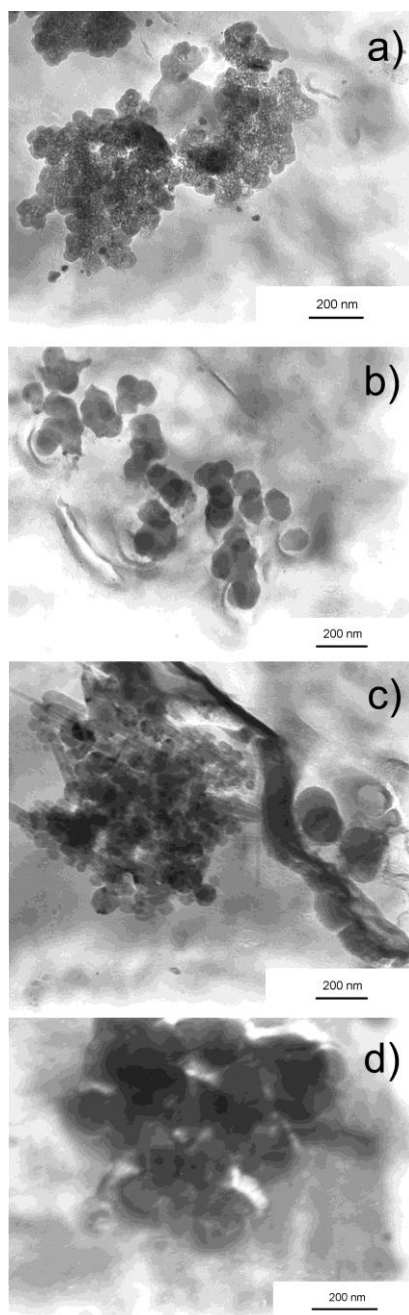


Figure 5. TEM images of the mechanically milled Ta (a) and mechanically alloyed Ta-5Nb (b), Ta-20Nb (c) and Ta-40Nb (d) nanocrystalline alloys

The hot-pressed alloys were investigated using AFM. The bulk samples were investigated approx. 1 mm under the original sample surface (samples were grinded and polished). The obtained AFM images (Fig. 6 and Fig. 7) have been shown using “deflection/error” signal, which enhances the visibility of the grain boundaries. Example AFM images with the grain size distributions for the Ta-W hot pressed alloys have been shown in Fig. 6. The smallest grains among all Ta-W alloys were formed in the Ta-10W alloy (c, d).

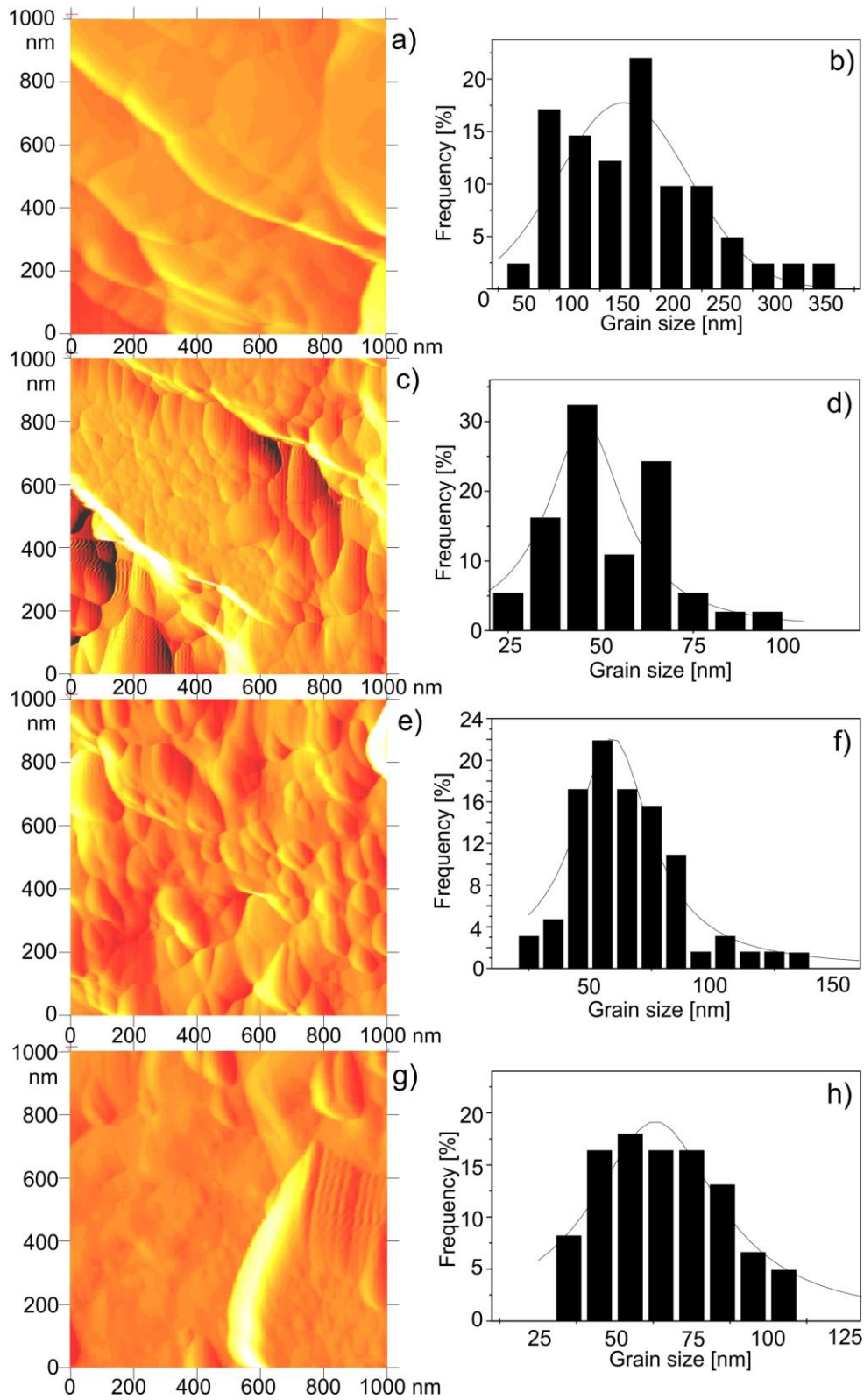


Figure 6. AFM images (a, c, e, g) and grain size distribution (b, d, f, h) of the hot-pressed Ta-xW alloys: Ta-5W (a, b), Ta-10W (c, d), Ta-20W (e, f) and Ta-40W (g, h)

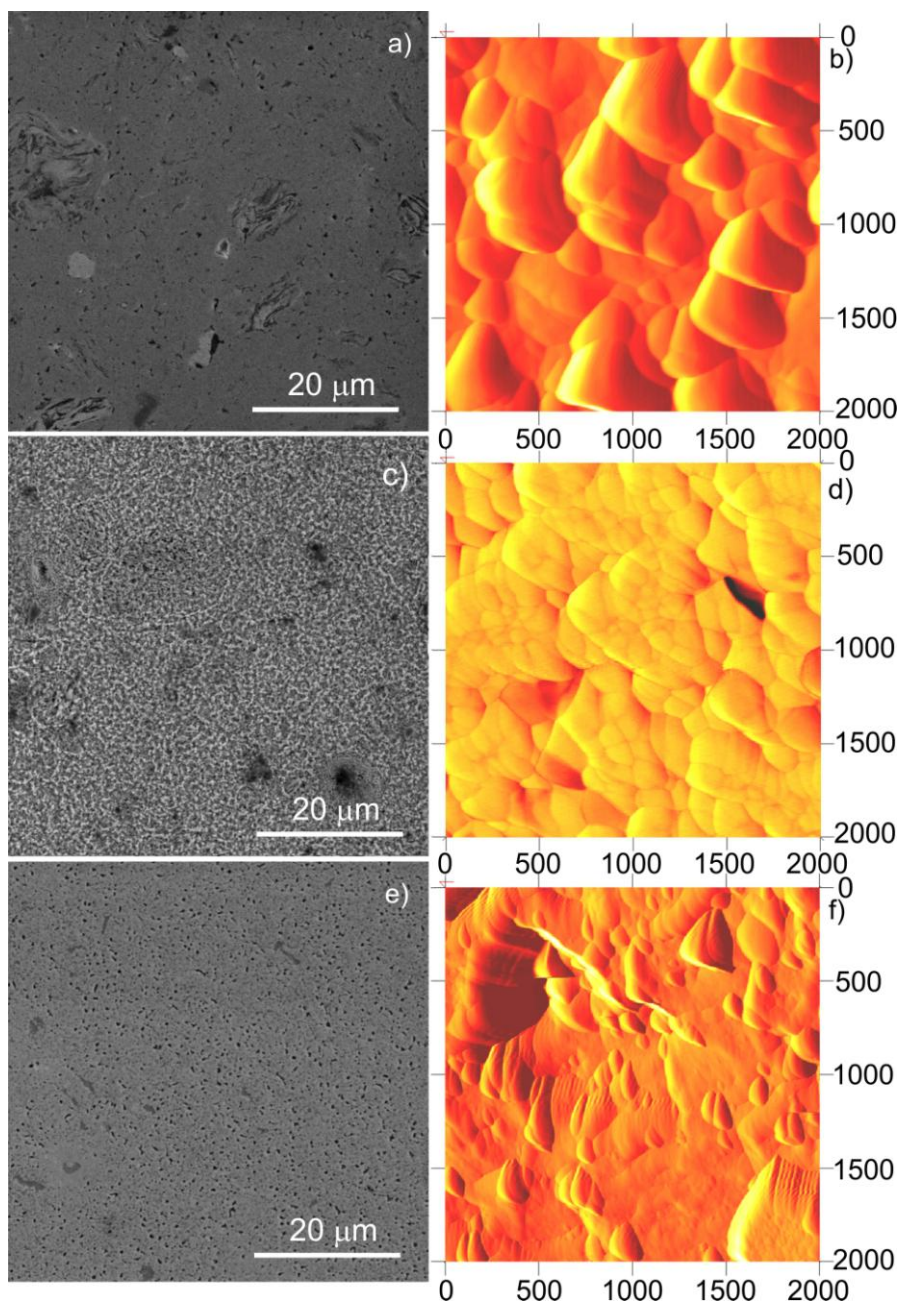


Figure 7. Example of SEM (a, c, e) and AFM (b, d, f) images of the Ta-40Nb (a, b), Ta-40 Mo (c, d) and Ta-40W (e, f) alloys after mechanical alloying and hot pressing

The comparison of the microstructure of the example Ta-40Nb (a, b), Ta-40Mo (c, d) and Ta-40W (e, f) alloys has been shown in Fig. 7. Both, SEM (a, c, e; lower magnification) and AFM (b, d, f; higher magnification) images have been shown, pointing to the difference in the grain size (at higher magnification) as well as the densification and residual porosity (at lower magnification) of the hot-pressed alloys. In the tantalum alloys, those that were modified by Nb, exhibit a larger grain size. The smallest grain size, measured by AFM, is representative of W doped alloys. The lowest and the smallest porosity and the pore size, respectively have alloys modified with tungsten. The Mo modified alloys have relatively the largest porosity. The density of the samples is approx. 93-95% of the theoretical value.

Based on the AFM images, the grain size distribution was determined for all alloy compositions and the results have been shown in Fig. 8. In the Ta-Nb alloys, the increased Nb content leads to a wider grain size distribution (not shown here). The alloy with 5% Nb has the narrowest grain size distribution with an average grain size of 128 nm. For 10% Nb, the average grain size is estimated to be 160 nm, whereas for 20% and 40% Nb, the average grain size is 190 and 195 nm, respectively. The Ta-Nb alloys have a relatively large and broad spectrum of the grain size (not shown here) from 30 to 350 nm. The largest grains were observed for a higher Nb content. In the Ta-Mo alloys, the grains are smaller in comparison to the Ta-Nb alloys. The smallest grains were observed for the 5% Mo content with an average value of 55 nm. The increased Mo content leads to an increased average grain size up to 155 nm. The increased Mo content also leads to a wider spectrum of the grain size distribution (not shown here) with the largest grains reaching 380 nm. In the Ta-W alloys, the 5% W does not lead to a grain size reduction as in the case of 5% Nb and 5% Mo, compared to pure Ta. For a higher W content, a significant reduction in the grain size was achieved and for Ta-10W a 45 nm average grain size was recorded. For 20% W and 40% W in the Ta alloy, the average grain size was 60 nm and 65 nm, respectively. For the Ta-W alloys, the grain size distribution was in the range from 20 to 350 nm. Generally, in all investigated alloys, the introduction of an alloying element results in a grain size reduction in a limited range. In alloys modified by Nb and Mo, the most significant reduction of the grain size was achieved for the 5-10% content, whereas for the W modified alloys, the most significant reduction of the grain size was achieved for 10-40% W. Tungsten is the most effective in grain size reduction. The results of the grain size, obtained using the AFM measurements, are roughly consistent with those measured by XRD or TEM.

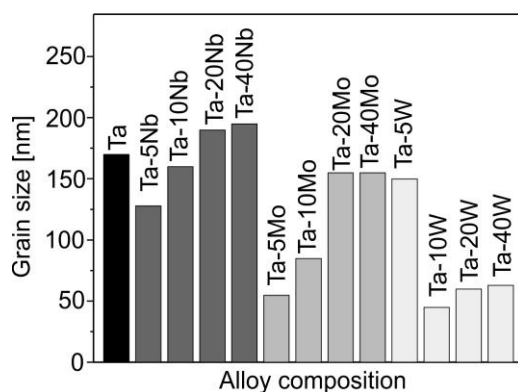


Figure 8. Average grain size for the Ta-xNb, Ta-xMo and Ta-xW alloys (x=0, 5, 10, 20, 40 wt.%); data obtained by AFM (not all AFM images and grain size distributions have been shown in this work)

The corrosion resistance was measured in chloride containing the Ringer's electrolyte and the results in the form of OCP-time dependence and polarization curves have been presented in Figs. 9-11 and in a qualitative form in Table 1. The measurement of stationary potential against time (OCP against time) determines the tendency of the material to corrode. Based on the OCP changes, the protective properties of the passive layer formed on the surface of the alloy can be estimated. Stationary potential measurement (OCP) is carried out in an open loop potentiostat. When the external

circuit is open, the current does not flow and the thermodynamic state is determined on the electrodes. The electrochemical cell is in the state of thermodynamic equilibrium.

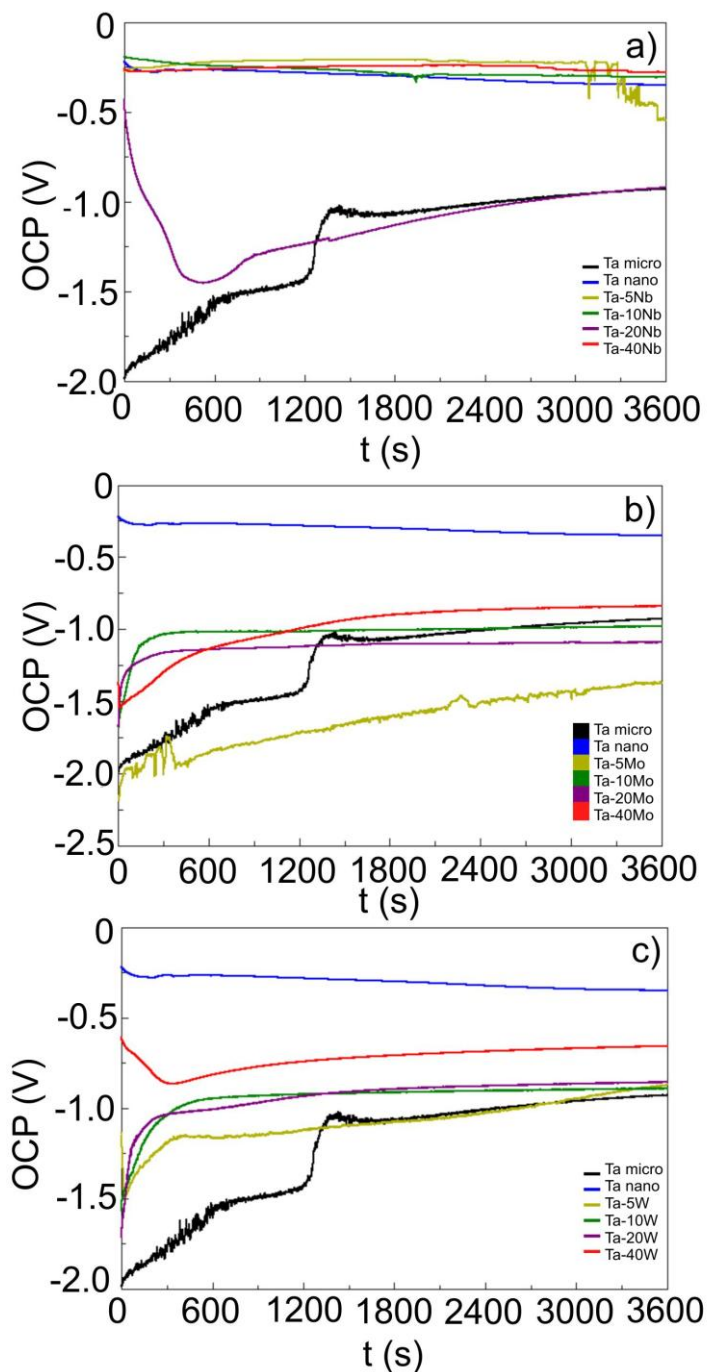


Figure 9. OCP as a function of time in the Ringer’s electrolyte for the Ta-xNb (a), Ta-xMo (b) and Ta-xW (c) nanocrystalline alloys (x=5, 10, 20, 40 wt.%); for comparison, data for nano- and microcrystalline Ta have been included

The open-circuit-potential (OCP) indicates a stabilization of the passive oxide layer (Fig. 9). The lowest negative OCP value represents microcrystalline tantalum, and for the investigated alloys, greatly shifts to a more positive one. Generally, the increase in the OCP with time for the Ta-W and

Ta-Mo alloys indicates a trend for passivation and thickening of the native oxide, while for pure nanocrystalline tantalum and most Ta-Nb alloys, the heavily stable passive layer does not form (a drop of the OCP). The example of the polarization curves has been shown in Fig. 10 and Fig. 11.

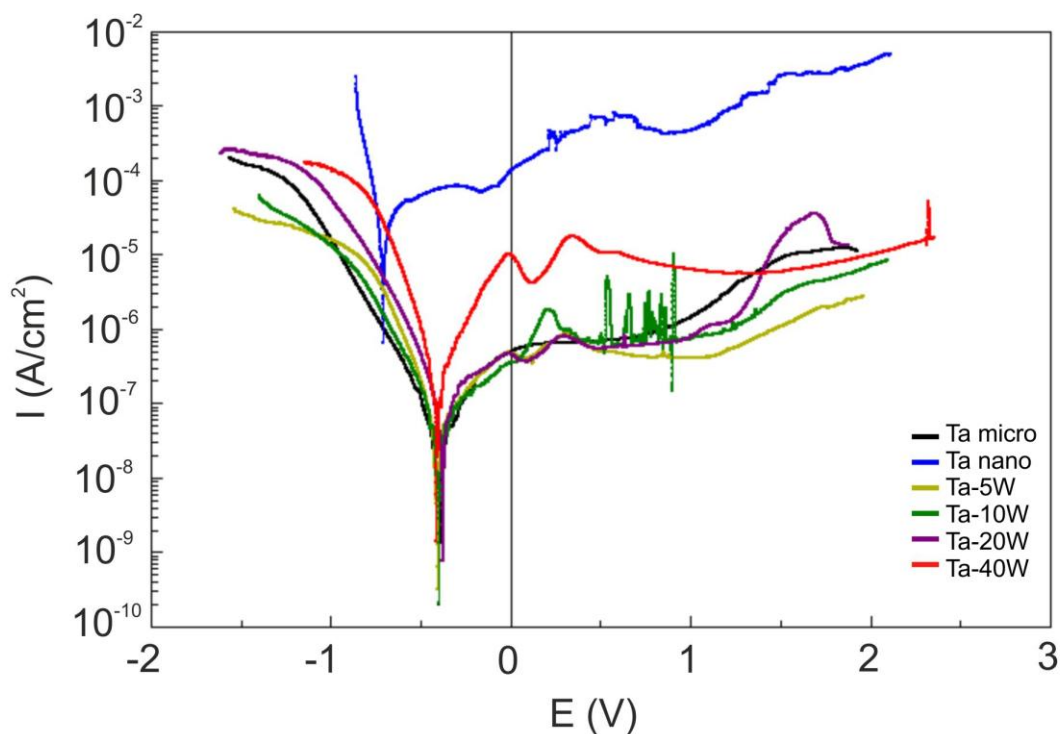


Figure 10. Polarization curves in the Ringer's electrolyte of the microcrystalline Ta, nanocrystalline Ta and nanocrystalline Ta-xW (x=5, 10, 20, 40 wt.%) alloys

Pure microcrystalline Ta (hot-pressed 325 mesh Ta powder) has a very good corrosion resistance. The corrosion current density (measured in the intersection of the Tafel tangent to the anodic and cathodic part of the polarization curve) was at the level of 10^{-8} A/cm² (Tab. 1). Hot-pressed pure nanocrystalline Ta has a significantly lower corrosion resistance and the corrosion current density was at the level of 10^{-5} A/cm². The deterioration of the corrosion resistance is the effect of a large volume of the grain boundaries and high internal energy of the nanocrystalline material. A modification of the chemical composition through an introduction of Nb, Mo and W affects the corrosion resistance. The Ta-10Nb nanocrystalline alloy has a better corrosion resistance by one order of magnitude in comparison to nanocrystalline pure Ta. For the other Nb containing alloys, no significant improvement or deterioration of the corrosion resistance was recorded. For the Ta-Mo alloys, the corrosion resistance was significantly better in comparison to the Ta-Nb alloys. For the Ta-5Mo nanocrystalline alloy the lowest corrosion current density of $1.173 \cdot 10^{-8}$ A/cm² was obtained (best corrosion resistance). The Ta-W alloys also exhibit a very high corrosion resistance. For the Ta-5W nanocrystalline alloy, the corrosion current density was $7.138 \cdot 10^{-8}$ A/cm². The Ta-Mo and Ta-W nanocrystalline alloys have the same level of corrosion current density I_{corr} as in the case of microcrystalline Ta and 3 orders of magnitude better than pure nanocrystalline Ta.

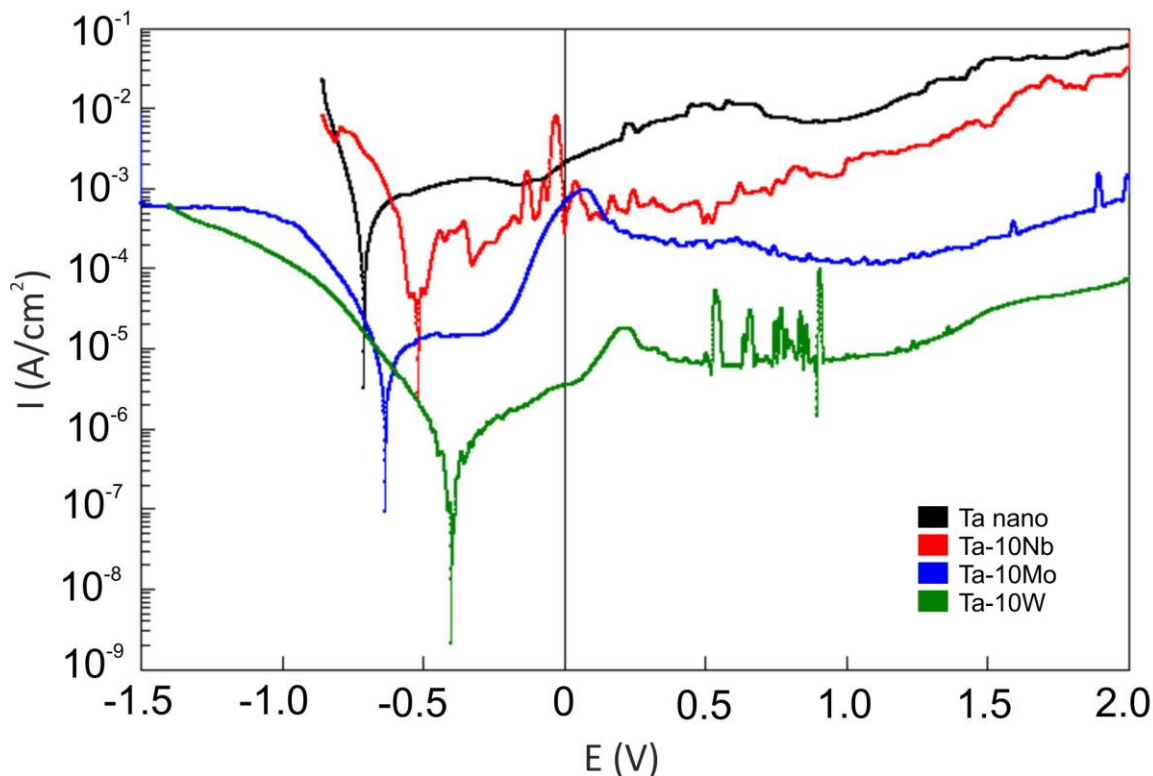


Figure 11. Polarization curves in the Ringer’s electrolyte of the nanocrystalline Ta, nanocrystalline Ta-10Nb, nanocrystalline Ta-10Mo and nanocrystalline Ta-10W alloys

Table 1. Corrosion current density I_{corr} , corrosion potential E_{corr} , passivation potential E_p , current of passivation I_{kp} , Flade potential E_F , transpassivation potential E_{tp} and current in the passive range I_p of the investigated hot-pressed Ta alloys

sample	I_{corr} [A/cm ²]	E_{corr} [V]	E_p [V]	I_{kp} [A/cm ²]	E_F [V]	E_{tp} [V]	I_p [A/cm ²]
Ta micro	$3.108 \cdot 10^{-8}$	-0.398	0.135	$6.166 \cdot 10^{-7}$	–	0.614	$7.134 \cdot 10^{-7}$
Ta nano	$1.198 \cdot 10^{-5}$	-0.711	-0.318	$1.298 \cdot 10^{-4}$	-0.160	–	–
Ta nano alloys:							
Ta-5Nb	$9.084 \cdot 10^{-5}$	-0.615	-0.364	$2.338 \cdot 10^{-4}$	0.081	–	–
Ta-10Nb	$5.852 \cdot 10^{-6}$	-0.519	–	–	–	–	–
Ta-20Nb	$9.182 \cdot 10^{-6}$	-1.023	-0.448	$5.717 \cdot 10^{-5}$	-0.187	-0.187	$5.268 \cdot 10^{-5}$
Ta-40Nb	$3.123 \cdot 10^{-5}$	-0.342	0.548	$4.205 \cdot 10^{-4}$	–	1.472	$5.57 \cdot 10^{-4}$
Ta-5Mo	$1.173 \cdot 10^{-8}$	-0.401	-0.351	$2.954 \cdot 10^{-7}$	–	–	–
Ta-10Mo	$4.201 \cdot 10^{-7}$	-0.635	-0.447	$1.626 \cdot 10^{-6}$	–	-0.278	$1.527 \cdot 10^{-6}$
Ta-20Mo	$1.778 \cdot 10^{-7}$	-0.587	–	–	–	-0.218	$9.673 \cdot 10^{-7}$
Ta-40Mo	$5.764 \cdot 10^{-8}$	-0.608	–	–	–	–	–
Ta-5W	$7.138 \cdot 10^{-8}$	-0.410	0.309	$8.601 \cdot 10^{-7}$	0.497	1.109	$4.222 \cdot 10^{-7}$
Ta-10W	$7.416 \cdot 10^{-8}$	-0.400	0.211	$1.812 \cdot 10^{-6}$	0.410	1.123	$8.383 \cdot 10^{-7}$
Ta-20W	$9.629 \cdot 10^{-8}$	-0.379	0.293	$7.948 \cdot 10^{-7}$	0.467	0.974	$7.276 \cdot 10^{-7}$
Ta-40W	$3.065 \cdot 10^{-7}$	-0.414	0.340	$1.742 \cdot 10^{-5}$	0.529	–	–

4. DISCUSSION

Refractory metals are classified as a group of metals of the melting temperature exceeding 2000°C. According to the melting temperature classification, pure refractory metals are: W, Re, Ta, Os, Mo, Ru, Ir, Nb, Hf, and Tc [28]. Only Mo, W, Ta, and Nb have important commercial applications in their pure form, whereas others have limited applications, due to limited availability and high cost, which is why, in this work, the alloy compositions based on the 4 above-mentioned elements were investigated.

The usual way for the alloy formation is conventional metallurgy, however significant differences in the melting temperatures constitute a problem in achieving high uniformity of the alloys. Alternatively, in this work an unconventional process of alloy synthesis was applied. In this process (mechanical alloying), the alloys were prepared from the elemental mixture of powders that were strongly deformed by the hitting balls in the milling reactor. The process of mechanical alloying eliminates the high temperature during alloy synthesis and the alloy formation takes place at room temperature, through mixing of powders, plastic deformation and cold welding. The heavy cold plastic deformation leads to a significant grain size reduction and uniform element distribution in the final powder mixture (Fig. 12). The final alloys are of high purity and the only impurity found was Fe (<2.1 wt.%), which originated in the milling vial (ball grinding). All alloying elements form a continuous solid solution. In the mechanical alloying, the final powders are in the form of agglomerates composed of nanograins. XRD, TEM and AFM provide comparable and complementary results of the grain size analysis. The microstructural analysis shows that mechanical synthesis is a good method to obtain nanocrystalline powders of designed composition.

Nanocrystalline powders are quite good candidates for consolidation and obtainment of bulk nanocrystalline metals. The nanocrystalline particles, owing to their very large surface area, should improve the densification process. The nanocrystalline particles, however, have a high cohesive force (large Van der Waals attraction force) resulting in the formation of agglomerates. Unfortunately, the agglomerates have significant voids between them, which may deteriorate densification [11]. The process of nanopowder consolidation requires the lowest possible temperature to avoid grain growth. Good choice is to use hot pressing, in which case the temperature, time and pressure are reduced in comparison to conventional powder metallurgy. Among different heating techniques, pulse plasma sintering (PPS) is one of the unconventional methods used for powder consolidation and grain growth reduction. The rising temperature during powder pressing improves densification and easier powder plastic deformation during compaction at a relatively low pressure, let alone reducing the voids between the consolidated powders. The high temperature contact of the reactive nanopowders with the graphite die and the punches leads to diffusion of carbon and formation of tantalum carbides during hot pressing. Instead of graphite, it is suggested to use a refractory metal [25]. The elevated temperature, however will limit the strength of the die. It is accepted that, for conventionally sintered microcrystalline powders, the temperature needed to achieve nearly full densification should be on the level of 0.8 of the melting temperature. Hence, for tantalum and its alloys, the sintering temperature should be over 2300°C [29].

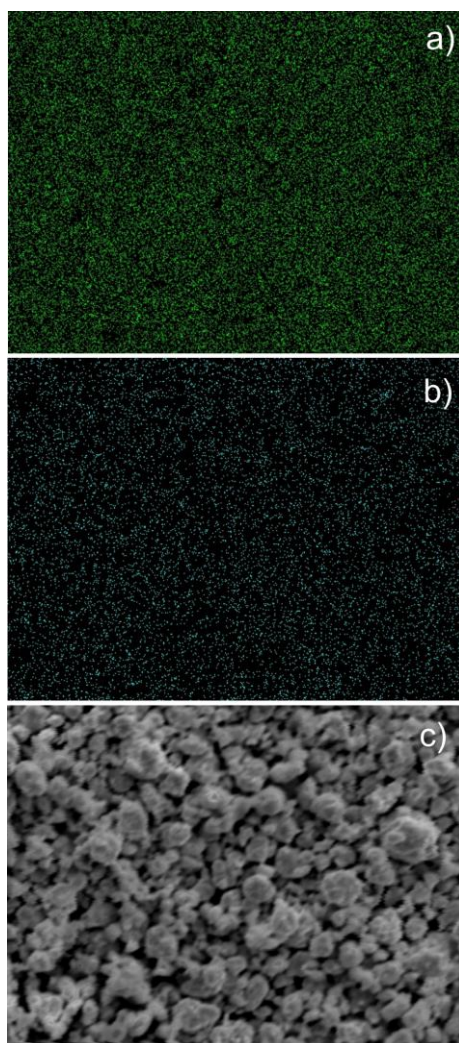


Figure 12. Example EDS map of the Ta (a) and W (b) distribution in the Ta-10W alloy powder after mechanical alloying (c)

For nanocrystalline or ultrafine-grained material densification, the consolidation temperature can be significantly lower [11, 24]. Additional reduction of the consolidation temperature can be achieved by the application of the hot pressing process [25]. The refractory alloying elements suppress grain growth during consolidation and, in this respect, out of the investigated alloys, tungsten exhibits the best behavior.

Tantalum has an extraordinary corrosion resistance. Tantalum is practically resistant in all concentrated and hot acidic environments [8]. Only 4% of the tantalum production, however, is used in the chemical industry for the production of corrosion resistant parts [8]. The limited use of tantalum in aggressive chemical environments is related to its high cost, which is approx. 10 and 5 times the cost of stainless steel and titanium for finished fabricated elements, respectively [30]. High corrosion resistance of tantalum is a consequence of the formation of a protective passive Ta_2O_5 oxide film. The stable oxides are formed during high temperature oxidation at temperatures in excess of 400°C . In other electrochemical surface treatment processes, the anodic oxidation would also lead to a formation of high quality oxide film. The anodic oxide has a significant thickness and cutoff of the aggressive

environments from pure metal background. The results of passivation are visible on the polarization curve. The oxidation of tantalum takes place in the reaction (eq.1) resulting in the most stable Ta₂O₅ oxide formation.



The Ta₂O₅ is the most stable oxide and the formation of unstable sub-oxides such as TaO or TaO₂ is unfavorable.

The open-circuit-potential (OCP) measurements are useful in determining of the material stability in aggressive liquids. Decreasing the OCP with time suggests dissolution of the protective tantalum oxide and surface activation [31]. An increase in the OCP to more positive values indicates the trend towards passivation, whereas a constant value denotes stabilization of the passive layer. The OCP can change over time along with the changes of the conditions in the electrochemical cell. This potential can be considered as corrosion potential E_{corr} as they are very similar, yet, during the measurement of the polarization curve, the obtained E_{corr} can deviate from the OCP because of various experimental parameters. The E_{corr} is therefore always taken from the polarization curve, not directly from the OCP and, hence the recorded different value of the OCP and E_{corr} (Figs. 9-11, Table 1).

In the conventional Ta-Nb alloys boiled in the H₂SO₄ solution, both α-Nb₂O₅ and β-Ta₂O₅ may form [8]. For a higher Ta content, only the Ta₂O₅ oxide forms and the material shows a higher corrosion resistance, whereas Nb deteriorates the corrosion resistance [8]. An increase in the alloying element (Nb, Mo or W) content in the Ta alloys leads to oxide composition changes, towards higher content of the oxide of the alloying element, for example Nb₂O₅ [8, 32]. The corrosion process carried out in the Ringer's electrolyte can lead to a reaction of the electrolyte components with the alloy elements and a formation of complex corrosion products (or oxide doped by Na⁺, K⁺, Ca²⁺, Cl⁻, which derive from the electrolyte) at higher anodic potentials. The nanostructure of high volume grain boundary can affect the corrosion products, due to a higher sensitivity to environments in comparison to the microcrystalline material of smaller volume grain boundary (this needs further investigations). The best corrosion resistance among the investigated alloys exhibit the Ta-W compositions. The Ta-Mo alloys also have very high corrosion resistance. The corrosion current density, which indicates the corrosion resistance, shows the lowest values (highest corrosion resistance) in the Ta-Mo and Ta-W system, comparable to those of microcrystalline pure Ta. Generally, the nanomaterials, due to a greater volume of the grain boundaries, have a lower corrosion resistance in comparison to their microcrystalline counterparts. In the case of the Ta-Mo and Ta-W alloys, the nanostructure shows a very good corrosion resistance and the problem of nanostructure was resolved in this matter.

5. CONCLUSIONS

This work discussed the formation and properties of the nanocrystalline Ta-xNb, Ta-xMo and Ta-xW alloys containing x = 5, 10, 20 and 40 wt.% of an additive element. The alloys were prepared using mechanical alloying, followed by hot pressing utilizing the pulse plasma sintering system. The structure, microstructure and corrosion resistance were investigated. The optimum properties for future applications in heavy working conditions exhibit the Ta-10W alloys, of the grain size of approx. 45 nm

and corrosion current density in the Ringer's electrolyte of $7.416 \cdot 10^{-8}$ A/cm². The nanocrystalline structure does not reduce the corrosion resistance in the Ta-Mo and Ta-W alloys, which is comparable to that of the microcrystalline pure Ta.

ACKNOWLEDGEMENTS

The work has been financed by National Science Centre, Poland under project identification DEC-2015/19/B/ST5/02595

References

1. B. E. Schuster, J. P. Ligda, Z. L. Pan and Q. Wei, *JOM*, 63 (2011) 27.
2. R. W. Buckman, *JOM*, 52 (2000) 40.
3. R. A. Silva, M. Walls, B. Rondot, M. Da Cunha Belo and R. Guidoin, *J. Mater. Sci. Mater. Med.*, 13 (2002) 495.
4. F. F. Schmidt, D. J. Maykuth and H. R. Ogden, *JOM*, 13 (1961) 487.
5. D. Gambale, *Adv. Mater. Processes.*, 168 (2010) 23.
6. S. M. Cordonne, P. Kumar, C. A. Michaluk and H. D. Schwartz, *Int. J. Refract. Met. Hard. Mater.*, 13 (1995) 187.
7. K. A. De Souza and A. Robin, *Mater. Chem. Phys.*, 103 (2007) 351.
8. A. Robin and J. L. Rosa, *Int. J. Refract. Met. Hard. Mater.*, 18 (2000) 13.
9. Y. J. Lee, T. H. Lee, D. Y. Kim, H. H. Nersisyan, M. H. Han, K. S. Kang, K. K. Bae, Y. J. Shin and J. H. Lee, *Surf. Coat. Technol.*, 235 (2013) 819.
10. T. E. Mitchell and P. L. Raffo, *Can. J. Phys.*, 45 (1967) 1047.
11. S. H. Yoo, T. S. Sudarshan, K. Sethuram, G. Subhash and R. J. Sowding, *Nanostruct. Mater.*, 12 (1999) 23.
12. J. B. Clark, R. K. Garrett, T. L. Jungling, R. Vandermeer and C. L. Vold, *Metall. Mater. Trans. A*, 22 (1991) 2039.
13. C. A. Michaluk, in *Tantalum*, Warrendale, TMS (1996) 205.
14. J. B. Clark, R. K. Garrett, T. L. Jungling and R. I. Asfahani, *Metall. Trans. A*, 22 (1991) 2959.
15. C. L. Briant, E. MacDonald, R. W. Balliet and T. Luong, *Int. J. Refract. Met. Hard. Mater.*, 18 (2000) 1.
16. V. Kentheswaran, S. Dine, D. Vrel, J. P. Couzinie and G. Dirras, *J. Alloys. Comp.*, 679 (2016) 80.
17. C. Hertl, L. Koll, T. Schmitz, E. Werner and U. Gbureck, *Mater. Sci. Eng. C*, 41 (2014) 28.
18. H. H. Nersisyan, J. H. Lee and C. E. Won, *Int. J. Self-Propag. High-Temp. Synth.*, 2 (2003) 149.
19. J. R. Groza and A. K. Zavaliangos, *Mater. Sci.*, 28 (2000) 171.
20. W. M. Goldberger and R. R. Fessler, in *Advances in Process Measurement for the Ceramic Industry*, New York, Wiley (1999) 337.
21. L. A. Stanciu, V. Y. Kodash and J. R. Groza, *Met. Mat. Trans.*, 10 (2001) 2633.
22. P. Angerer, E. Neubauer, L. G. Yu and K. A. Khor, *Int. J. Refract. Met. Hard. Mater.*, 25 (2007) 280.
23. M. Dias, F. Guerreiro, J. B. Correia, A. Galatanu, M. Rosiński, M. A. Monge, A. Munoz, E. Alves and P. A. Carvalho, *Fusion. Eng. Des.*, 98-99 (2015) 1950.
24. Z. Fang, P. Maheshwari, X. Wang, H. Y. Sohn, A. Griffio and R. Riley, *Int. J. Refract. Met. Hard. Mater.*, 25 (2005) 249.
25. Y. Kim, E. P. Kim, J. W. Noh, S. H. Lee, Y. S. Kwon and I. S. Oh, *Int. J. Refract. Met. Hard. Mater.*, 48 (2015) 211.
26. J. Jakubowicz and M. Sopata, Structure and microstructure of high-energy ball-milled nanocrystalline tantalum, *Ann. Int. Conf. on Mater. Sci. Metal and Manufact.*, Singapore (2017) 1.

27. L. Smardz, K. Smardz, M. Jurczyk and J. Jakubowicz, *J. Alloys. Comp.*, 313 (2000) 192.
28. R. Morales, R. E. Aune, O. Grindler and S. Seetharaman, *JOM*, 55 (2003) 20.
29. R. M. German, *Sintering Theory and Practice*, John Wiley and Sons, (1996).
30. F. J. Hunkeler, in *Refractory Metals and Their Industrial Applications ASTM International*, Philadelphia, (1984) 28.
31. K. A. De Souza and A. Robin, *Mater. Lett.*, 57 (2003) 3010.
32. S. Komiyama, E. Tsuji, Y. Aoki, H. Habazaki, M. Santamaria, F. Di Quarto, P. Skeldon and G. E. Thompson, *J. Solid State Electrochem.*, 16 (2012) 1595.

© 2018 The Authors. Published by ESG (www.electrochemsci.org). This article is an open access article distributed under the terms and conditions of the Creative Commons Attribution license (<http://creativecommons.org/licenses/by/4.0/>).